WARSAW UNIVERSITY OF TECHNOLOGY Index 351733
FACULTY OF CIVIL ENGINEERING
COMMITTEE FOR CIVIL AND WATER ENGINEERING
POLISH ACADEMY OF SCIENCES ISSN 1230-2945

DOI: 10.24425/ace.2025.155091
ARCHIVES OF CIVIL ENGINEERING
Vol. LXXI ISSUE 3 2025

pp. 145 –163

Research paper

Research on the shrinkage performance and pore characteristics of flexible solidified silt based on solid waste

Xianjin Xu[1], Lei Zhang[2], Shuai Liu[3], Shutao Meng[4], Chao Li[5], Zhaoyun Sun[6], Jincheng Wei[7], Hongbo Zhang[8]

Abstract: This study aimed to verify the effect of solidification materials based on solid waste on the shrink-age performance of silt, the main raw materials of solid waste were red mud, zeolite powder, and matrix asphalt. Temperature shrinkage and drying shrinkage tests were conducted to compare and analyze the shrinkage characteristics using three kinds of solidification materials (2%, 4%, and 6%), with 6% cement-solidified soil and plain soil used as control. The results showed that the solidification material based on solid waste effectively reduced the temperature shrinkage strain and temperature shrinkage coefficient of soil; moreover, the material had good resistance to temperature shrinkage deformation. A drying shrinkage test showed that the addition of solidification materials based on solid waste considerably improved the early water retention capacity of the test soil. The water loss process mainly occurred in the first 7 days of the test. Meanwhile, the addition of the solidification material considerably reduced the drying shrinkage strain and drying shrinkage coefficient of the test soil, and the effect was more obvious as the content amount increased. Through NMR and CT scanning tests, the pore size and pore volume of the solidified material mixed with solid waste were found to be significantly reduced. The dominant pore size ranged from 0.01 µm to 1 µm. The solidification material based on solid waste improved the crack resistance of the soil, providing a new reference measure for subgrade and roadbed fillers, as well as a new means for the recycling of solid waste.

Keywords: solid waste, flexible solidified silt, shrinkage property, aperture characteristics

---

[1] PhD., Eng., Qilu Expressway Company Limited, Jinan 250102, China, e-mail: 2998344186@qq.com, ORCID: 0009-0003-6158-9445

[2] PhD., Eng., Shandong Transportation Institute, Jinan 250102, China, e-mail: realchungsdu@163.com, ORCID: 0009-0007-9339-3331

[3] PhD., Eng., Qilu Expressway Company Limited, Jinan 250102, China, e-mail: 985852383@qq.com, ORCID: 0009-0000-2490-8361

[4] PhD., Eng., RoadMainT Company Limited, Beijing 100191, China, e-mail: 837827723@qq.com, ORCID: 0009-0001-6704-5444

[5] PhD., Eng., Qilu Expressway Company Limited, Jinan 250102, China, e-mail: 2214759384@qq.com, ORCID: 0009-0002-4640-6754

[6] PhD., Eng., Shandong Transportation Institute, Jinan 250102, China, e-mail: andersontwo@163.com, ORCID: 0000-0001-5214-3351

[7] PhD., Eng., Shandong Transportation Institute, Jinan 250102, China, e-mail: weijincheng@sdjtky.cn, ORCID: 0009-0003-4614-7569

[8] PhD., Eng., Shandong University, Jinan 250002, China, e-mail: zhanghongbo@sdu.edu.cn, ORCID: 0000-0003-2204-4584

1. Introduction

Silt is a poor soil that cannot be used directly in highway construction projects, and it is typically improved with cement and other materials to meet performance requirements. However, the hydration reaction of cement consumes a large amount of water, leading to an easy occurrence of a drying shrinkage strain and a temperature shrinkage strain in the cement–soil mixture, which affects the overall strength and stability of the road [1–3].

Numerous industrial wastes, such as red mud, tailings, and steel slag are produced during industrial production. The stacking of these industrial wastes seriously affects the surrounding ecological environment. It is crucial to promote environmental protection and sustainable economic and social development as a way of addressing the environmental pollution and potential safety problems caused by improper disposal and stockpiling of bulk industrial solid waste. These efforts can be made from the perspectives of industrial waste reduction, recycling, and reuse. Meanwhile, red mud, tailings, steel slag, and other industrial wastes often meet the basic physical and mechanical requirements of road filling materials, and many scholars [4–8] have used these materials in road engineering projects. Therefore, resources are recycled while engineering costs are minimized through the use of these materials to develop new road building materials and their large-scale application in highway engineering construction. Red mud has a porous structure, a large specific surface area, and strong adsorption. It can be used to clean gas and treat sewage [9–12].

Alkan G [14] analyzed the chemical and mineral composition of red mud and found that the chemical composition mainly consists of SiO_2 and Cao, including a small amount of Al_2O_3 and Fe_2O_3, and the mineral composition mainly consists of nepheline, boehmite, and diaspore, with its physical properties similar to those of silty clay. Cao Ying et al. [15] studied the solidification of red mud using phosphogypsum (dosage of 10–15%) as the active ingredient. The study found that the red mud was alkaline, had good activation ability for fly ash, and enhanced its activity. Qin Lusheng [16] conducted experiments to study the red-mud base material of Shandong Aluminum Industry Co., Ltd. and found that the red-mud road-base material mixed in the ratio of red mud:fly ash:cement = 80:10:10 had higher strength and a greater rebound value, which meet the requirements of high-grade highways. Gaurav Pande [17] reduced the amount of cement by increasing the amount of silica fume, reduced the leaching of fluoride and other pollutants in red mud, and also reduced the pH value. Sun Zhaoyun [18] prepared a red-mud, asphalt-powder curing agent using the sintering method and verified its good curing performance.

Bituminous materials are complex mixtures of hydrocarbons and their derivatives of different molecular weights, which are temperature-sensitive materials with flowing self-healing properties [19–22]. The asphalt changes its state at room temperature to form a large specific surface area, which is fully mixed with the silt particles and dispersed among them. As the temperature rises, the asphalt softens, further filling the pores and micro cracks [23, 24]. This phenomenon improves the material's compressive strength and shear strength, makes the entire material semi flexible, and realizes the function of self-healing and reinforcement for the micro damage of the material [25].

Alvaro Garcia [26] analyzed the healing process of asphalt using the theory of capillary mechanics, established a capillary flow model, and proposed the hypothesis that under appropriate temperature conditions, the capillary flow in asphalt microcracks leads to crack closure, and the interface strength gradually recovers because of the diffusion of interface molecules. Kim [27] showed that the chemical composition and structure of asphalt have a vital impact on its self-healing performance. Asphalt containing a large number of small molecules or light, long structural molecules has a strong self-healing ability; moreover, a high aromatic hydrocarbon content promotes asphalt healing and recovery. The increase in the content of heteroatoms such as sulfur, oxygen, and nitrogen enhances the polarity of asphalt and increases its viscosity, which hinders its self-healing and recovery. The interactions between the long-chain hydrocarbons in wax and aliphatic molecules cause the adsorption of van der Waals forces, which promotes asphalt healing [28–30].

Silt has a low clay content, poor particle grading, high permeability, and significant water sensitivity. The strength and stiffness of silt can be improved with traditional inorganic materials such as cement and lime. However, certain problems persist, including poor water resistance, poor frost resistance, drying shrinkage, and temperature shrinkage cracking. In this study, a flexible solidification material based on red mud and asphalt was developed using inorganic and organic composite methods. Silt solidification significantly improves the water resistance and frost resistance of silt, reducing the degree of dry shrinkage and temperature shrinkage cracking through the adequate improvement of the silt strength and stiffness.

2. Materials

2.1. Silt

The basic physical parameters of the silt used in this article were determined through compaction tests and limit water content tests performed on the soil obtained from a certain Yellow River floodplain area in Shandong, as shown in Table 1.

Table 1. Basic physical properties of silt

Maximum Dry Density ($g{\cdot}cm^{-3}$)	**Optimum Water Content (%)**	**Liquid Limit (%)**	**Plastic Limit (%)**	**Soil Classification**
1.79	13.93	29.66	19.93	Low-Liquid-Limit Silt Soil

An analysis of the basic physical properties of the silt showed that $W_L < 50$, and $IP = 9.73$. According to the classification criteria of soil [31], the soil sample can be classified as low-liquid-limit silt soil.

2.2. Cement

The cement used in this study was ordinary P.O42.5 Portland cement. The basic properties of the selected cement were tested, and the following performance indicators were obtained in Table 2.

Table 2. Physical and mechanical property indexes of cement

Density ($g \cdot cm^{-3}$)	**Specific Surface Area ($m^2 \cdot kg^{-1}$)**	**Compressive Strength (MPa)**		**Flexural Strength (MPa)**	
		3 d	**28 d**	**3 d**	**28 d**
3.18	369.7	6.8	8.9	36.3	55.8

2.3. Flexible curing material

A flexible curing material (Fig. 1), an anti-shrinkage soil curing agent, was developed in black powder with a particle size of less than 0.075 mm. The main raw materials used for production were red mud, zeolite powder, and 70 # matrix asphalt. The red mud used was a Bayer process red mud; the main mineral components were SiO_2, Fe_2O_3, Al_2O_3, and CaO, with mass ratios of 9.58%, 2.45%, 21.7%, and 43.15%, respectively. The penetration of 70 # matrix is 70 (0.1 mm), and the softening point is 46.5°C. The curing material mix ratio was red mud: zeolite powder: 70# matrix asphalt = 22 : 1 : 100.

Fig. 1. Flexible curing material

3. Test methods

3.1. Curing agent ratio

To verify the influence of flexible solidification materials on the shrinkage performance of soil, as well as the effectiveness, three proportions of solidification materials and cement were designed to modify the soil. Meanwhile, the improved soil and that with only cement added were used as control groups. The specific test scheme is presented in Table 3.

Table 3. Test scheme

Combinations	**Cement (%)**	**Flexible Curing Material (%)**	**Silt (%)**
FC-0	6	0	100
FC-2	6	2	100
FC-4	6	4	100
FC-6	6	6	100
S-0	0	0	100

3.2. Compaction test

According to the test scheme, compaction tests were conducted on each experimental plan to obtain the maximum dry density and optimal moisture content. The compaction results of each plan are presented in the Table 4.

Table 4. Compaction test data

Combinations	**Maximum Dry Density (g· cm^{-3})**	**Optimum Water Content (%)**
FC-0	1.98	16.78
FC-2	1.93	14.03
FC-4	1.78	14.22
FC-6	1.83	14.35
S-0	1.79	13.93

3.3. Specimen preparation

A center beam specimen with a size of 10 cm × 10 cm × 40 cm was selected. According to the compaction test, the maximum dry density and optimal moisture content of the material were obtained, and the material was compacted and formed with a compaction degree of 96%. The formed specimen was placed in a standard curing room and maintained for seven days under standard curing conditions of 20°C ± 2°C and humidity ≥ 95%. On the last day of the curing period, the specimen was soaked in water.

3.4. Temperature shrinkage test

After the specimens were completely cured, each was placed in the oven and baked at a constant temperature until no free water remained in the specimen. After drying, the specimen was placed in a dry and ventilated place to air at room temperature. The specimen was moved into a high- and low-temperature alternating test chamber, and the temperature control program was set to start from 50°C, reducing at a step of 10°C until reaching –10°C; the cooling rate was 0.5°C/min when the temperature dropped to the set temperature. After setting the temperature, the oven was kept warm for 3 h. The dial indicator reading was taken within 5 min before the end of the holding period.

The temperature shrinkage performance is usually represented by the temperature shrinkage coefficient (α_T), which refers to the linear shrinkage coefficient of a material under unit temperature change. The formulas are to be referred to as Eq. (3.1).

$$\alpha_T = \frac{\Delta\varepsilon}{\Delta T} \tag{3.1}$$

where: ΔT – the amount of temperature change (°C); $\Delta\varepsilon$ – the change in strain corresponding to ΔT (%).

3.5. Drying shrinkage test

After the specimen preparation, the specimen was cured for 7 days according to the standard curing method and soaked in water on the last day of the curing period. The surface of the saturated specimen was wiped dry and placed on a drying shrinkage instrument in a constant temperature and humidity test chamber to measure the drying shrinkage deformation of the specimen. Meanwhile, the same specimen was placed in the constant-temperature and humidity test chamber to measure the drying shrinkage water loss rate, and the temperature and humidity in the test chamber were controlled to 20°C and 60%, respectively.

Dry shrinkage performance is usually evaluated by indicators such as dry shrinkage strain and dry shrinkage coefficient. The calculation formulas of dry shrinkage strain and dry shrinkage coefficient are as Eq. (3.2) and Eq. (3.3).

$$\varepsilon_d = \frac{\delta_d}{L} \tag{3.2}$$

$$\alpha_d = \frac{\varepsilon_d}{\omega} \tag{3.3}$$

where: ω – the water loss rate of the specimen (%); ε_d – the dry shrinkage strain of the specimen (%); δ_d refers to the overall shrinkage of the specimen when the water loss is ω (mm).

3.6. Nuclear magnetic resonance (NMR) test

To analyze the evolution law of the pore structure of flexible solidified silt, nuclear magnetic resonance (NMR) tests were performed on FC-6 (composite-stabilized silt samples) using the pq-001 mini NMR nuclear magnetic resonance analyzer. Cylindrical stabilized silt samples with a diameter of 50 mm and a height of 100 mm were selected for the tests. The transverse relaxation time T_2 of the saturated soil samples was tested after 1 d, 3 d, 7 d, 14 d, and 28 d curing ages to determine the evolution law of the pore distribution characteristics of the stabilized silt samples with increasing curing ages. The samples were vacuumed and saturated for 12 hours prior to the NMR tests.

3.7. CT scan test

The samples were also scanned using a Zeiss Xradia 510versa X-ray imager. The samples of silt (S-0), cement-solidified silt (FC-0), and flexible solidified silt (FC-6) were scanned, and the changes in the pore structure of the different samples were compared and analyzed.

4. Results

4.1. Temperature shrinkage test results

As shown in Fig. 2, the variation pattern of the temperature shrinkage coefficient was relatively consistent among different materials. The temperature shrinkage coefficient increased with decreasing temperature. When the temperature range was between 10°C and 0°C, the temperature shrinkage coefficient exhibited a decreasing trend, and when the temperature range was between 0°C and –10°C, the temperature shrinkage coefficient showed an increasing trend. The shrinkage of the soil with temperature change was mainly caused by the volume changes of the solid and liquid phases within the material. As the temperature decreased, the water remaining in the pores of the material was lost, and the tension in the meniscus in the capillaries was reduced. Consequently, the original structural balance within the pores was lost, increasing the coefficient of temperature shrinkage for the material. When the temperature dropped to approximately 0°C, the moisture in the capillary tube of the material changed from the liquid to solid state, and the volume increased; this phenomenon caused a resistance to the internal coupling force of part of the capillary wall particles, decreasing the temperature shrinkage coefficient. As the temperature dropped further to –10°C, the coupling force between the particles within the capillary wall continued to increase, and the temperature shrinkage coefficient also increased as a consequence.

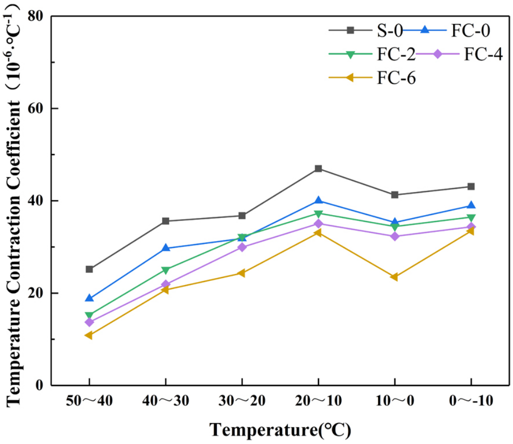

Fig. 2. Variation of temperature shrinkage coefficient with temperature

The average value of the material's temperature shrinkage coefficient in each temperature range reflects the overall level of the material's shrinkage characteristics with respect to temperature changes.

As shown in Fig. 3, Scheme S-0 had the largest average temperature shrinkage coefficient, and that of Scheme FC-0 was 14.9% lower, with the average temperature shrinkage coefficient of flexible solidified soil being the smallest. This result shows that cement and a flexible curing agent have a significant improvement effect on the temperature shrinkage coefficient of soil. For flexible solidified soil, as the dosage increased, the temperature shrinkage coefficient reduced, and the flexible curing agent had a more obvious increasing effect on the temperature shrinkage performance of the material. Compared with Scheme S-0, the average temperature shrinkage coefficient of scheme FC-6 dropped by 36.2%, and the improvement effect was more obvious than that of Scheme FC-0.

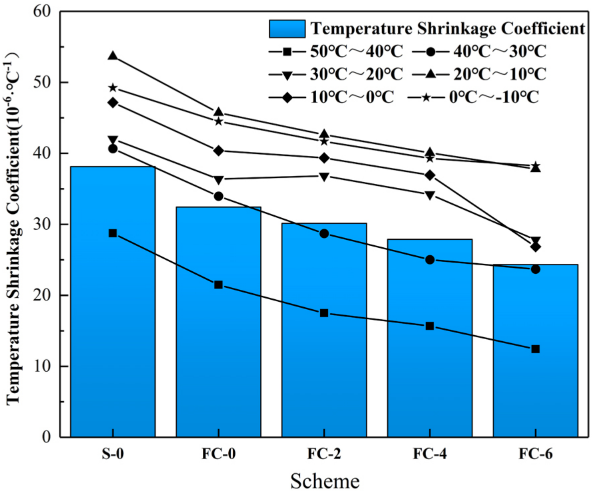

Fig. 3. Comparison of temperature shrinkage coefficients of different schemes

4.2. Drying shrinkage test results

4.2.1. Water loss rate

Time is an important factor in the water loss of soil. As soil water was lost through the voids and capillary pores of the samples, their overall volume decreased while they shrank; hence, the water retention degree of the materials is an important indicator to measure their shrinkage performance. As shown in Fig. 4, the entire water loss process can be approximately divided into three stages: surface water loss stage, internal gravity flow loss stage, and capillary water loss stage. For the different materials, the initial stage of water loss was mainly the surface water loss stage, and the water loss in this stage was the largest; in the internal gravity flow loss stage, the water loss increased with time and the rate of change slowed down; in the capillary water loss stage, the rate of change of the water loss rate tended to be milder.

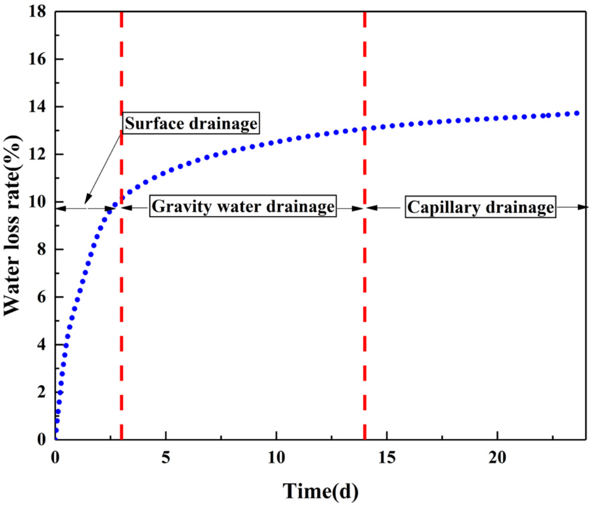

Fig. 4. The stage of water loss process

As shown in Fig. 5, in terms of the total duration of the water loss process, Scheme S-0 had the shortest duration of 12 days; the duration of Schemes FC-2 to FC-6 did not vary significantly with the dosage, both of which were approximately 24 days. Although Scheme FC-0 took the longest time, being 28 days, its final water loss rate was the highest, reaching 16.5%, indicating poor water retention of cementitious soil.

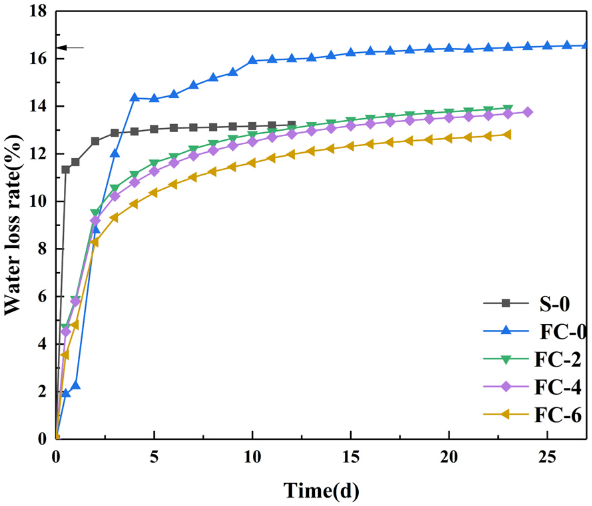

Fig. 5. Comparison of final water loss rates

The water loss rate of Scheme S-0 changed considerably at the early stage, that is, the water loss rate of the silt reached 11.65% on the first day of the experiment, ac-counting for 88% of the final water loss rate. However, the relationship between water loss rate and time in the other four schemes was relatively consistent, as they all showed substantial changes within the first 7 days. As time increased, the water loss rate gradually stabilized or slightly increased. The silt specimen had better initial water retention and suppressed the generation of shrinkage cracks in the specimen to some extent, compared with the case of Scheme S-0. On the seventh day, for cement soil Scheme FC-0, the water loss rate reached 89.9%. For flexible solidified soil, the water loss rate of Scheme FC-2 reached 87.5%, Scheme FC-4 reached 86.6%, and Scheme FC-6 reached 85.5%. As the amount of flexible curing agent increased, the final water loss rate decreased, and its water retention performance was enhanced. Therefore, during construction, maintenance measures should be taken within 7 days after completion to avoid excessive water loss leading to increased shrinkage strain.

4.2.2. Shrinkage strain

Figure 6 shows that the variation behavior of the drying shrinkage strain of Scheme S-0 differed from that of other materials. At the early stage of Scheme S-0, the drying shrinkage strain changed most obviously, which mainly occurred 2 days before the drying shrinkage test, and the drying shrinkage strain reached 89.5% of the total strain. The drying shrinkage strain gradually slowed down with time and finally stabilized at 12 days; the drying shrinkage strain of Scheme FC-0 and Schemes FC-2–FC-6 showed the same trend with time. The drying shrinkage strain mainly occurred in the first 14 days of the test, and on the 14th day, the drying shrinkage strain exceeded 85% of the total strain. The drying shrinkage strain gradually stabilized with time.

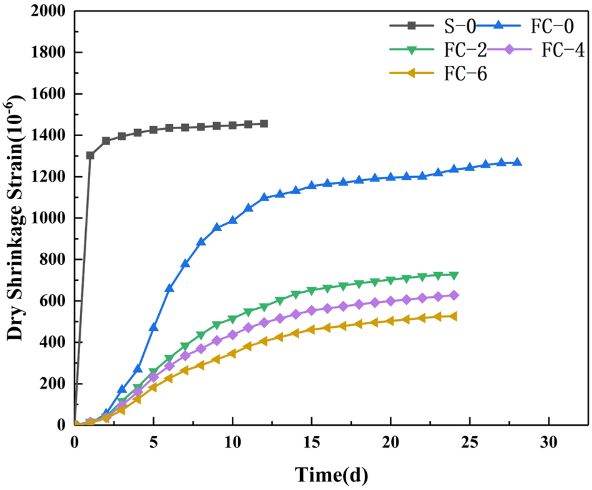

Fig. 6. Variation of drying shrinkage strain with time

A comparison of the overall drying shrinkage strain and average drying shrinkage coefficient of the three materials, as shown in Fig. 7, shows that FC-6 < FC-4 < FC-2 < FC-0 < S-0, indicating that both cement soil and flexible solidified soil can effectively inhibit the increase in drying shrinkage strain, and the effect of the flexible curing agent is better. The higher the dosage, the better the effect. According to the water loss rate and time variation, it can be concluded that the flexible solidified soil had good early water retention and considerably reduced the drying shrinkage strain of silt.

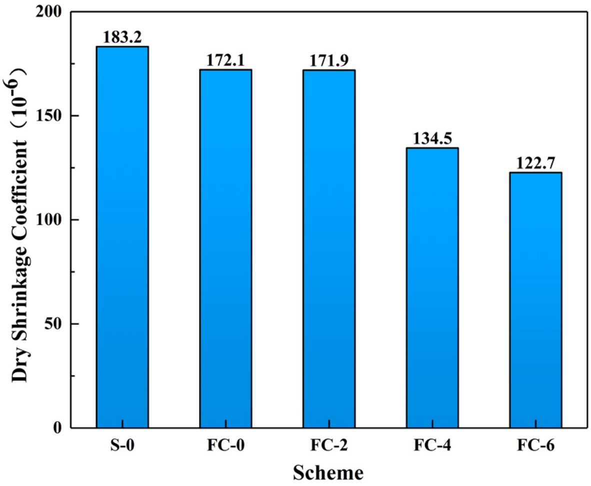

Fig. 7. Comparison of average drying shrinkage coefficients of various schemes

4.3. Aperture characteristics in T_2 spectrum

The shrinkage property of a material is strongly related to its internal pore structure. To analyze the evolution law of the pore structure of the flexible solidified silt, an NMR test was conducted on the FC-6 sample. According to the NMR theory, when the porous medium is completely saturated, the transverse relaxation time T_2 of a single pore is directly proportional to the ratio of the surface area (S) and volume (V) of the pore. Therefore, the distribution of T_2 obtained from the soil sample test can be used to convert the pore size distribution characteristics of the soil sample.

The T_2 distribution curve of the stable curing at different ages is shown in Fig. 8. To identify the pore size corresponding to the T_2 distribution curve, pores with a transverse relaxation time T_2 of 0.1 ms to 10 ms are classified as micropores, and those with a T_2 of 10 ms to 100 ms are classified as macropores. The T_2 distribution curve of the solidified silt at different ages follows a bimodal distribution. To facilitate the analysis of the test results, the signal peaks on the left and right sides of the T_2 distribution curve are defined as the main peak and secondary peak, respectively.

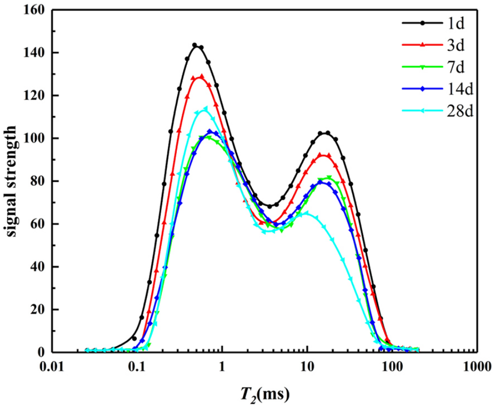

Fig. 8. T_2 distribution curve of stable curing at different ages

In general, as the curing age increased, the maximum value of the main peak increased before 14 days but decreased significantly at 28 days. The maximum value of the secondary peak gradually shifted to the lower left with increasing age. This phenomenon shows that a positive correlation exists between T_2 and pore size, and the integral area of the curve of the T_2 spectrum is the total pore volume. Therefore, considering the change trend of the T_2 distribution curve with age, it can be concluded that the proportion of macropores in the solidified silt samples decreased with age, while the proportion of micropores increased with age. This indicates that after adding the curing agent, the hydration products in the samples continuously increased with age. The bonding and filling effects of the hydration products resulted in a gradual decrease in the volume and quantity of the macropores, some of which transformed into micropores, resulting in an overall increase in the proportion of micropores in the sample.

From the relaxation mechanism of NMR, three types of relaxation exist for fluids in porous media: transverse volume (free) relaxation, transverse surface relaxation, and diffusion relaxation. Studies on the pore water in soil media showed that the effects of free and diffusive relaxations on the relaxation time T_2 were negligible. Moreover, the T_2 value of the pore water in the soil samples was only related to the internal structural pores of the soil. The formulas are to be referred to as Eq. (4.1)

$$\frac{1}{T} = P_2\frac{S}{V} = F_s\frac{P_2}{r} \tag{4.1}$$

where: r – the pore size (µm), F_s – he pore shape factor, the spherical pore is 3, the columnar pore is 2, P_2 – the transverse relaxation rate, and the transverse relaxation rate of silt is 325 µm/s.

To accurately evaluate the variation pattern of the pore size of flexible solidified silt during early maintenance, the T_2 corresponding to the peak in the T_2 distribution curve is characterized as the dominant pore size in the soil sample. Simplifying the value of F_s in Eq. (4.1) to (4.2), Eq. (4.1) can be transformed into Eq. (4.2):

$$r = 2P_2T_2 \tag{4.2}$$

As shown in Table 5 and Fig. 9, the dominant pore size of the macropores decreased with curing age, while the dominant pore size of the micropores increased continuously with curing age. This phenomenon can be explained as follows: the increase in curing age was accompanied by the gradual filling of the soil pores by the hydration products of cement, which gradually reduced the size of the macropores and decreased the overall number of pores.

Table 5. The dominant pore size of flexible solidified silt at different curing ages

Curing ages	Dominant pore size of micropores (µm)	Dominant pore size of macropores (µm)
1d	0.090	3.915
3d	0.095	3.865
7d	0.125	3.405
14d	0.130	2.560
28d	0.130	1.890

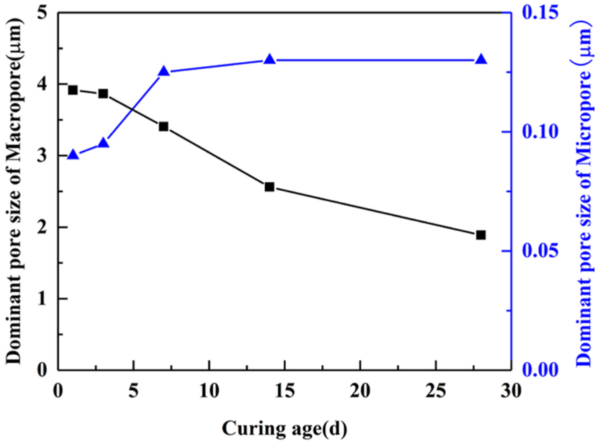

Fig. 9. Variation of dominant pore size of stabilized silt with curing age

As shown in Fig. 10, the pore diameter distribution ranged from 0.01 µm to 10 µm. With the increase in curing age, the proportion of the pore volume with a pore size of 2.5 µm to 10 µm decreased, and the pores with a size of 0.01 µm to 1 µm gradually became the dominant pores. As shown in Fig. 10. Variation of pore size distribution Fig. 11. Variation of accumulated pore volume the cumulative pore volume decreased with the increase in curing age, and the accumulated pore volume of the stabilized silt decreased from 55.3 cm^3 to 40.1 cm^3 after 28 days of curing.

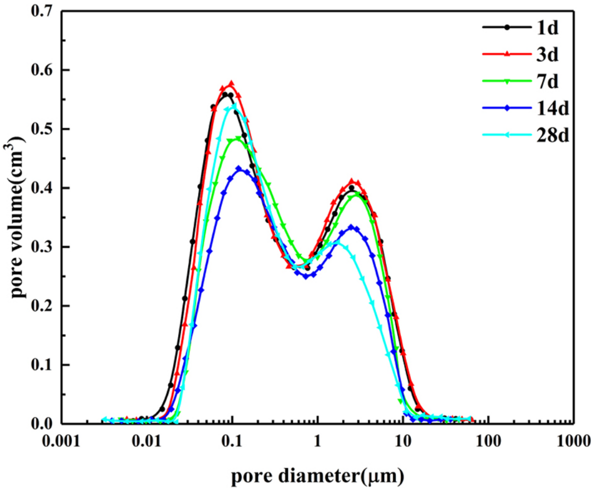

Fig. 10. Variation of pore size distribution

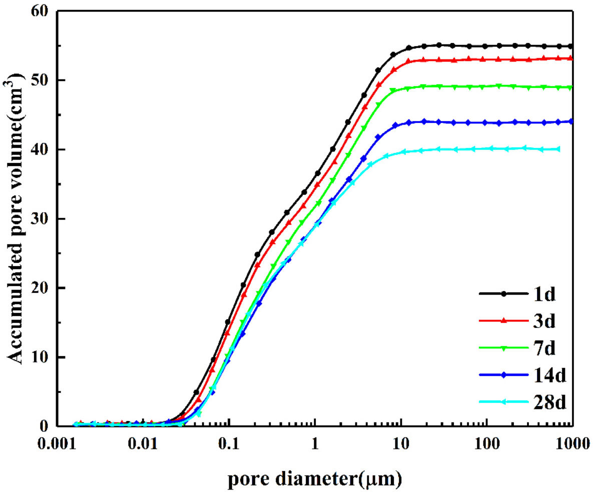

Fig. 11. Variation of accumulated pore volume

4.4. CT 3D imaging analysis

The three-dimensional structure of the samples was reconstructed using an image analysis software, and the structure and pore characteristics of different silt specimens before and after solidification were analyzed. Owing to the differences in the X-ray absorption rates because of different densities, the CT image after scanning was presented in two parts: a high-density soil matrix part and a low-density porous part. Hence, the pore structure of the sample was statistically analyzed using the built-in shape analysis function of the software.

The resolution of the CT image was 1.28 µm, and the 3D images and pore distribution of the reconstructed soil sample are shown in Fig. 12. The 3D images show considerable differences in the pore morphology of the soil aggregates, with pores of different sizes existing in the aggregates. Also observable are numerous macropores, elongated or irregularly rectangular pore shapes, and small round and elongated pores. The pores of the cement-cured silt are evenly distributed, the pores of different pore sizes are distributed, and the macropores are different. The 3D diagram of the soft-cured silt is dominated by small pores whose distribution pattern results in a compact and dense aggregate structure, which is consistent with the results of the shrinkage performance measurements.

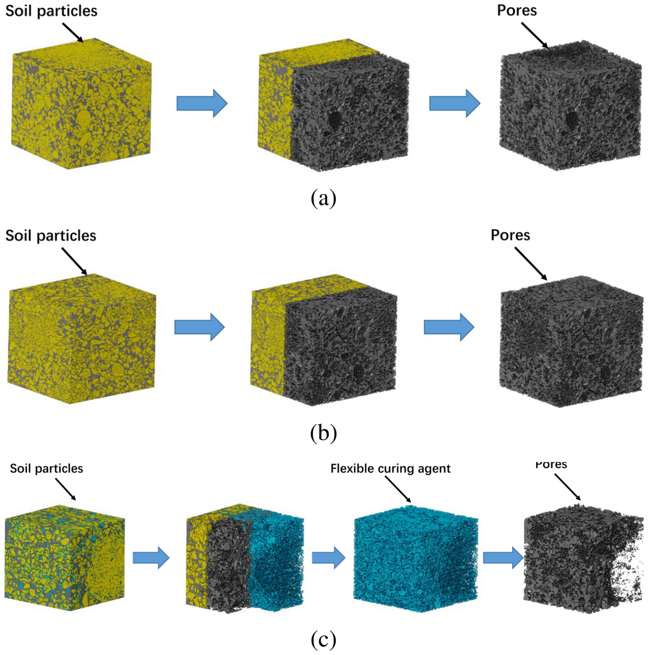

(a)

(b)

(c)

Fig. 12. Three-dimensional reconstruction of CT scan: (a) Silt, (b) Cement-cured silt, (c) Flexible solidified silt

The pore diameter distribution mainly ranged from 0.01 µm to 15 µm. According to the pore size, the aggregate pores were divided into four grades: 0–5, 5–10, 10–15, and > 15 µm. Meanwhile, the differences in the pore size distribution of the soil aggregates of silt, cement-solidified silt, and flexible solidified silt were compared, as shown in Fig. 13. The figure shows that the increase in the flexible curing materials is followed by a downward macropore trend, a decrease in the proportion of the 10–15 µm pores from 44% to 12%, and a significant increase in small pores < 5 um from 13% to 38%. This result is consistent with the results of the NMR, and the aggregates of the softly cured silt have a smaller pore distribution, indicating that the aggregates have a good structure, stronger stability, and better mechanical properties and durability.

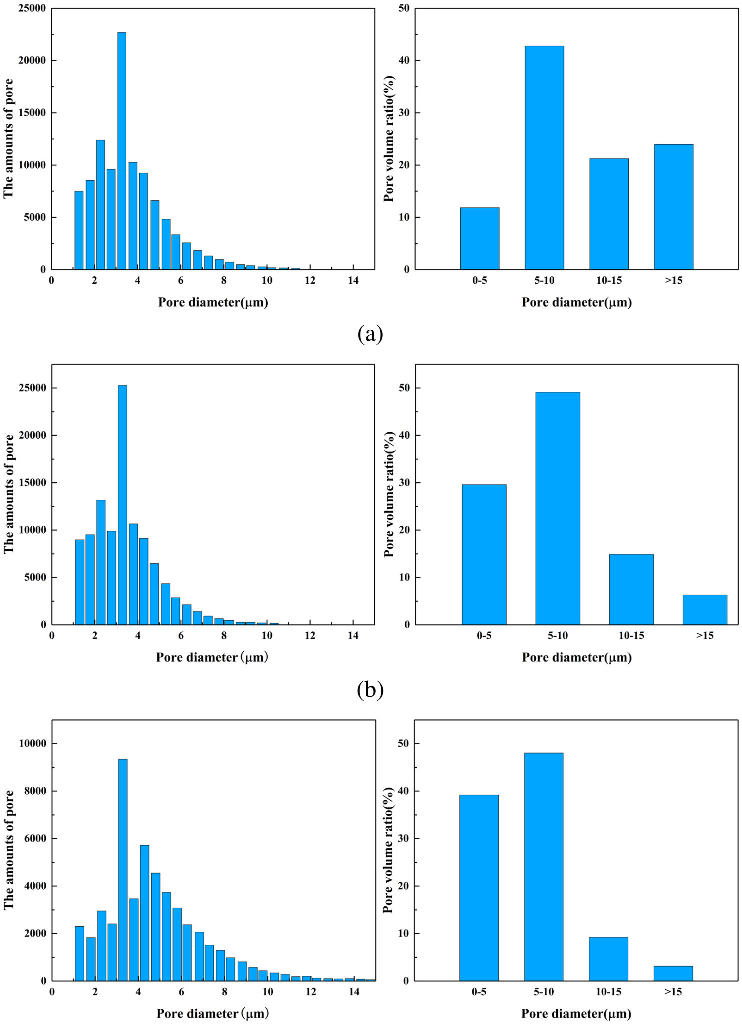

(a)

(b)

(c)

Fig. 13. The pore distribution of CT scan: (a) Silt, (b) Cement-cured silt, (c) Flexible -solidified silt

5. Conclusions

In this study, the shrinkage performance of a flexible-soil-solidified material based on solid waste was investigated. The following conclusions were obtained:

1. Adding a flexible curing agent based on solid waste can effectively improve the temperature shrinkage characteristics of soil and reduce the temperature shrinkage strain and temperature shrinkage coefficient; the improvement effect also increases with increasing dosage;

2. Temperature shrinkage tests showed similarities among the temperature shrinkage variation behaviors of various materials. As temperature decreases, the temperature shrinkage coefficient initially increases, which is followed by a decrease and then an increase. The temperature shrinkage coefficient increases with a decrease in temperature. When it reaches the temperature range of 10°C to 0°C, the temperature shrinkage coefficient decreases. At the temperature range of 0°C to –10°C, the temperature shrinkage coefficient increases again;
3. The stabilized soil mixed with a flexible curing agent based on solid waste and cement can significantly improve the early water retention capacity of soil, and the water loss process mainly occurs within the first 7 days of the test. Therefore, maintenance measures should be taken within 7 days after construction is completed to avoid excessive water loss that increases drying shrinkage strain;
4. An analysis of the relationship between drying shrinkage and time showed that plain soil had the shortest time, being 12 days, and mainly occurred 2 days before the drying shrinkage test. The time for flexible solidified soil was 24 days, and that for cement soil was 28 days, which mainly occurred in the first 14 days of the drying shrinkage test;
5. According to the NMR test, the pore diameter distribution range is 0.01 μm to 10 μm. The increase in curing age is accompanied by a decrease in the volume proportion of pores having a size of 2.5 μm to 10 μm, with the pores having a size of 0.01 μm -1 μm gradually becoming the dominant pores.
6. Through a CT scanning test, the aggregates of the flexible solidified silt were found to have a smaller pore distribution, indicating that the aggregates had a good aggregate structure and better mechanical properties and durability.

References

[1] S.A. Saleh, S.K. Hussein, and G.J. Khoshnaw, "Effect of Soil Stabilization on Subgrade Soil Using Cement, Lime and Fly Ash", *Eurasian Journal of Science and Engineering*, vol. 6, no. 2, pp. 39–52, 2020, doi: 10.23918/eajse.v6i2p39.

[2] M.R. Sun, L. Zhang, J.Y. Shang, J. Xu, and J.J. Yang, "Influence of Cement and Aggregate Content on Physical Properties of Soil Base Material", *Building Technology Development*, vol. 46, no. 22, 2019.

[3] Q. Wang, H. Chu, W. Shi, J. Jiang, and F. Wang, "Feasibility of preparing self-compacting mortar via municipal solid waste incineration bottom ash: an experimental study", *Archives of Civil and Mechanical Engineering*, vol. 23, no. 4, art. no. 251, 2023, doi: 10.1007/s43452-023-00794-5.

[4] L. Zhong, Y. Zhang, and Y. Zhang, "Extraction of alumina and sodium oxide from red mud by a mild hydro-chemical process", *Journal of Hazardous Materials*, vol. 172, no. 2-3, pp. 1629–1634, 2009, doi: 10.1016/j.jhazmat.2009.08.036.

[5] L.Y. Li, "Properties of red mud tailings produced under varying process conditions", *Journal of Environmental Engineering*, vol. 124, no. 3, pp. 254–264, 1998, doi: 10.1061/(ASCE)0733-9372(1998)124:3(254).

[6] A.I. Cakici, J. Yanik, S. Uçar, T. Karayildirim, and H. Anil, "Utilization of red mud as catalyst in conversion of waste oil and waste plastics to fuel", *Journal of Material Cycles and Waste Management*, vol. 6, pp. 20–26, 2004, doi: 10.1007/s10163-003-0101-y.

[7] R.G. Courtney and J.P. Timpson, "Reclamation of fine fraction bauxite processing residue (red mud) amended with coarse fraction residue and gypsum", *Water, Air, and Soil Pollution*, vol. 164, pp. 91–102, 2005, doi: 10.1007/s11270-005-2251-0.

[8] A.P. He, Z. L. Hu, D.G. Cao, J. M, Zeng, B.L. Wu, and L.J. Wang, "Extraction of Valuable Metals from Red Mud", *Advanced Materials Research*, vol. 881–883, pp. 667–670, 2014, doi: 10.4028/www.scientific.net/amr.881-883.667.

[9] E. Kalkan, "Utilization of red mud as a stabilization material for the preparation of clay liners", *Engineering Geology*, vol. 87, no. 3–4, pp. 220–229, 2006, doi: 10.1016/j.enggeo.2006.07.002.

[10] Y. Zhao, N. Liang, H. Chen, and Y. LI, "Preparation and properties of sintering red mud unburned road brick using orthogonal experiments", *Construction and Building Materials*, vol. 238, art. no. 117739, 2020, doi: 10.1016/j.conbuildmat.2019.117739.

[11] M. Patel, "Extraction of titanium dioxide& production of building bricks from red mud", *Research and Industry*, vol. 37, pp. 154–157, 1992.

[12] Q. Ma, W. Duan, X. Liu, P. Fang, R. Chen, T. Wang, and Z. Hao, "Engineering Performance Evaluation of Recycled Red Mud Stabilized Loessial Silt as a Sustainable Subgrade Material", *Materials (Basel)*, vol. 15, no. 9, art. no. 3391, 2022, doi: 10.3390/ma15093391.

[13] P.E. Tsakiridis, S. Agatzini-Leonardou, and P. Oustadakis, "Red mud addition in the raw meal for the production of Portland cement clinker", *Journal of Hazardous Materials*, vol. 116, no. 1-2, pp. 103–110, 2004, doi: 10.1016/j.jhazmat.2004.08.002.

[14] G. Alkan, B. Yagmurlu, S. Cakmakoglu, T. Hertel, Ş. Kaya, L. Gronen, and B. Friedrich, "Novel Approach for Enhanced Scandium and Titanium Leaching Efficiency from Bauxite Residue with Suppressed Silica Gel Formation", *Scientific Reports*, vol. 8, no. 1, art. no. 5676, 2018, doi: 10.1038/s41598-018-24077-9.

[15] Y. Cao, W.D. Li, and Y.G. Liu, "Properties of Red Mud and Current Situation of Its Utilization", *Bulletin of the Chinese*, vol. 26, no. 1, pp. 143–145, 2007.

[16] L. Qin, Q. Nie, H. Zhang, X. Jia, and C. Zhang, "Laboratory experimental study on red mud geopolymer used as road subgrade materials", *E3S Web of Conferences*, vol. 261, art. no. 02043, 2021, doi: 10.1051/E3SCONF/202126102043.

[17] G. Pande, S. Selvakumar, C. Ciotonea, J.M. Giraudon, J.F. Lamonier, and V.S. Batra, "Modified red mud catalyst for volatile organic compounds oxidation", *Catalysts*, vol. 11, no. 7, art. no. 838, 2021, doi:10.3390/catal11070838.

[18] Z.Y. Sun, H. Wu, and J.I. Hou, "Study on Construction and Quality Evaluation for Subgrade Filling of Red Mud in Modified Bayer Process", *Subgrade Engineering*, no. 3, pp. 69–72, 2018.

[19] D. Sun, G. Sun, X. Zhu, Q. Pang, F. Yu, and T. Lin, "Identification of wetting and molecular diffusion stages during self-healing process of asphalt binder via fluorescence microscope", *Construction and Building Materials*, vol. 132, pp. 230–239, 2017, doi: 10.1016/j.conbuildmat.2016.11.137.

[20] J. Qiu, M. van de Ven, S. Wu, J. Yu, and A. Molenaar, "Evaluating self healing capability of bituminous mastics", *Experimental Mechanics*, vol. 52, pp. 1163–1171, 2012, doi: 10.1007/s11340-011-9573-1.

[21] D. Grossegger and A. Garcia, "Influence of the thermal expansion of bitumen on asphalt self-healing", *Applied Thermal Engineering*, vol. 156, pp. 23–33, 2019, doi: 10.1016/j.applthermaleng.2019.04.034.

[22] Y. Hou, L. Wang, T. Pauli, and W. Sun, "Investigation of the asphalt self-healing mechanism using a phase-field model", *Journal of Materials in Civil Engineering*, vol. 27, no. 3, 2015, doi: 10.1061/(asce)mt.1943-5533.0001047.

[23] A. Garcia, E. Schlangen, and M. Van de Ven, "Two ways of closing cracks on asphalt concrete pavements: microcapsules and induction heating", *Key Engineering Materials*, vol. 417-418, pp. 573–576, 2009, doi: 10.4028/www.scientific.net/kem.417-418.573.

[24] D. Sun, L. Zhang, and G. Liang, "Review on self-healing behavior of asphalt concrete (1) mechanism and characterization methods of self-healing behavior", *Petroleum Asphalt*, vol. 5, no. 4, 2011.

[25] B.R. Anupam, U.C. Sahoo, and A.K. Chandrappa, "A methodological review on self-healing asphalt pavements", *Construction and Building Materials*, vol. 321, art. no. 126395, 2022, doi: 10.1016/j.conbuildmat.2022.126395.

[26] Á. García, "Self-healing of open cracks in asphalt mastic", *Fuel*, vol. 93, no. 1, pp. 264–272, 2012, doi: 10.1016/j.fuel.2011.09.009.

[27] Y.R. Kim, D.N. Little, and F.C. Benson, "Chemical and mechanical evaluation on healing mechanism of asphalt concrete (with discussion)", *Electronic journal of the Association of Asphalt Paving Technologists*, vol. 59, 1990.

[28] A. Schmets, N. Kringos, T. Pauli, P. Redelius, and T. Scarpas, "On the existence of wax-induced phase separation in bitumen", *International Journal of Pavement Engineering,* vol. 11, no. 6, pp. 555–563, 2010, doi: 10.1080/10298436.2010.488730.

[29] D.N. Little, R.L. Lytton, D. Williams, and Y.R. Kim, “An analysis of the mechanism of microdamage healing based on the application of micromechanics first principles of fracture and healing”, *Journal of the Association of Asphalt Paving Technologists*, vol. 68, 1999.

[30] A. García, J. Norambuena-Contreras, and M.N. Partl, “Experimental evaluation of dense asphalt concrete properties for induction heating purposes”, *Construction and Building Materials*, vol. 46, pp. 48–54, 2013, doi: 10.1016/j.conbuildmat.2013.04.030.

[31] JBG 3430-2020 Test Methods of Soils for Highway Engineering. Beijing, China: Architecture and Building Press, 2020.

Received: 2024-04-02, Revised: 2024-07-09